Electromagnetic control of an oscillating turbulent jet in a confined cavity

Righolt, Bernhard; Kenjeres, Sasa; Kalter, Rudi; Tummers, Mark; Kleijn, Chris

DOI
10.1016/j.ijheatfluidflow.2016.09.007

Publication date
2016

Document Version
Accepted author manuscript

Published in
International Journal of Heat and Fluid Flow

Citation (APA)
Righolt, B., Kenjeres, S., Kalter, R., Tummers, M., & Kleijn, C. (2016). Electromagnetic control of an oscillating turbulent jet in a confined cavity. *International Journal of Heat and Fluid Flow*, *62*(Part B), 395-406. https://doi.org/10.1016/j.ijheatfluidflow.2016.09.007

Electromagnetic control of an oscillating turbulent jet in a confined cavity

B. W. Righolt[a,b], S. Kenjereš[a,b], R. Kalter[a,b], M. J. Tummers[c,b], C. R. Kleijn[a,b]

[a]*Section Transport Phenomena, Department of Chemical Engineering, Faculty of Applied Sciences, Delft University of Technology, Delft, Van der Maasweg 9, 2629HZ, Netherlands*
[b]*J. M. Burgerscentre for Fluid Mechanics*
[c]*Laboratory for Aero and Hydrodynamics, Delft University of Technology*

Abstract

Control of self-sustained jet oscillations in confined cavities is of importance for many industrial applications. It has been shown that the mechanism underlying these oscillations consists of three stages: (i) growth of the oscillation, (ii) amplitude limitation and (iii) delayed destruction of the recirculation zone bounding the jet. It has also been shown that oscillations may be enhanced or suppressed by applying (e.g. electromagnetic) body forces.

In the current paper we study the influence of electromagnetic forces oriented aligned with or opposite to the direction of the jet on the oscillation mechanism. The influence of the forcing is found to depend on the Stuart number N in relation to a critical Stuart number N_{crit}. We demonstrate that for $|N| < N_{crit}$, the oscillation mechanism is essentially unaltered, with moderate modifications in the jet oscillation amplitude and frequency compared to $N = 0$. For $N > N_{crit}$, electromagnetic forcing leads to total suppression of the self-sustained oscillations. For $N < N_{crit}$, electromagnetic forces dominate over inertia and lead to strongly enhanced oscillations, which for $N \ll -N_{crit}$ become irregular.

As was earlier demonstrated for $N = 0$, the present paper shows that for $-6N_{crit} < N < N_{crit}$ the oscillatory behaviour, i.e. frequencies, oscillation amplitudes and wave shapes, can be described quantitatively with a zero-dimensional model of the delay differential equation (DDE) type, with model constants that can be *a priori* determined from the Reynolds and Stuart number and geometric ratios.

1. Introduction

In continuous steel casting, in which liquid steel from a tundish is injected into a thin mould through an injection tube with tailored nozzle configuration,[1, 2] an even distribution of heat is important in order to achieve uniform solidification and high quality steel.[3, 4] Flow turbulence and large scale self-sustained flow oscillations [5, 6] may have a large detrimental impact on the temperature distribution and steel quality.[7] Both can be well controlled by means of an

electromagnetic brake (EMBr), [8, 9, 10] where electric currents are induced by the magnetic field.

Electromagnetic forcing of conductive fluids is also achieved by the simultaneous application of imposed electric currents and external magnetic fields. Electromagnetic forcing via induced or imposed electrical currents can enhance or suppress self-sustained jet oscillations,[6] enhance wall-heat transfer by increased turbulent mixing,[11, 12] control flows near boundaries,[13, 14] in order to reduce drag,[15, 16, 17] or to control the boundary layer thickness,[18, 19] which influences flow separation. [20, 21]

Although in many industrial applications complicated nozzle configurations with multiple injected jets are commonly used,[1, 2] most of the relevant mechanisms determining flow stability are also present, and can be studied more generically, in a single jet configuration.[22, 6] A single jet injected into a thin confined cavity exhibits self-sustained oscillations above a critical Reynolds number, depending on the width to nozzle diameter ratio.[23] These oscillations are found in a large range of jet Reynolds numbers, i.e. $100 < Re < 170,000$.[6, 24, 25, 26, 27, 28] For given jet Reynolds number, increasing the cavity width leads to a decreasing oscillation frequency,[29] until the oscillation vanishes.[30]

As a follow up to our earlier paper [10], in which we experimentally demonstrated the effect of electromagnetic control on jet flow oscillations in thin cavities, in the present paper we present a systematic analysis of the influence of electromagnetic body forces on single jet oscillations in a confined cavity, using Large Eddy computational fluid flow simulations and theoretical analyses of the zero-dimensional system dynamics in combination with our earlier experimental data. We impose the Lorentz force as a body force to enhance and suppress these oscillations. The objective of this paper is to (i) study the fundamental flow regimes introduced by imposing an EMBr on a single jet oscillation, (ii) investigate the similarities between the self-sustained jet oscillation mechanism with and without application of an EMBr, (iii) demonstrate that flow oscillations in thin cavities in the presence of EMBr forcing can be described by a zero-dimensional model of the Delay Differential Equation (DDE) type.

The paper is outlined as follows. The electromagnetically controlled jet configuration, a description of the electromagnetic forcing and the numerical methods used to simulate these are given in section 2, the physical mechanisms underneath the self-sustained oscillation in the presence of an EMBr are discussed in section 3. Section 4 describes a zero-dimensional model for electromagnetically controlled single jet oscillations in a confined cavity, and section 5 discusses the details of the model parameters and demonstrates the applicability of the model.

2. Problem definition and methods

2.1. Description of the set-up

Figure 1 depicts the configuration of a thin liquid filled cavity that we study in this paper. The cavity has dimensions $H \times W \times T = 0.7 \times 0.3 \times 0.035$ m^3 and

was previously studied experimentally using planar particle imaging velocimetry (PIV) [6], as well as numerically for varying width W using Large Eddy Simulations (LES). In [23] we also proposed a zero-dimensional model that predicts the amplitude and frequency of self-sustained jet oscillations in thin liquid filled cavities as a function of the jet Reynolds number and geometric ratios. A square nozzle of size $d = 0.01$ m is submerged to a depth $d_n = 0.1$ m underneath the free liquid surface and injects the fluid with a velocity v_{in} into the cavity. The electrically conducting fluid in the domain has density $\rho = 1.1 \times 10^3$ kgm^{-3}, viscosity $\nu = 1.27 \times 10^{-6}$ m^{2}s^{-1} and conductivity $\sigma = 7.1$ Sm^{-1}. These properties correspond to the working fluid used in the experiments of the previous studies.[6]

In the present work, we apply electromagnetic forcing as a body force for the control of the jet motion. We follow the design by Kalter et al. [6] and place two electrodes on opposite sides of the cavity, at a distance L below the nozzle exit with a potential difference $\Delta\phi = \phi_1 - \phi_2$. These electrodes are centered in the z-direction and have an area of $A = 0.03 \times 0.03$ m^2. A direct current I flows either from left to right ($I > 0$) or from right to left ($I < 0$) between both electrodes. Furthermore, we place three magnets in the top of the domain, just underneath the nozzle exit against the outside of the back wall. The magnets are aligned with their centers at $y = -0.15$ m and $z = -0.045$ m and separated by a distance $D = 0.08$ m. The poles of the magnets are facing in alternating direction. Appendix A lists the details of this electromagnetic field. The directions of the resulting Lorentz forces are also depicted in Figure 1 and can be flipped by changing the direction of the electrical current. Later we will show that this leads to an enhancement or suppression of the oscillations.

In Figure 1(left) we indicate the jet angle θ, which is defined from a least squares fit of a line $x(y)$ through the points $(x_i, y_i, z = 0)$ defined by $x_i = \max_x(|v(y_i, z = 0)|)$ and $(-d_n - S) < y_i < (-d_n)$, where we choose $S = W$. Furthermore, the two monitoring points, p_1 and p_2 are defined on opposite sides of the jet.[23]

2.2. Dimensionless numbers

In this work we define the Reynolds number, Re, the Stuart number, N, and the Strouhal number, St, as

$$Re = \frac{v_{in} d}{\nu}, \qquad N = \frac{B_{ref} dI}{\rho A v_{in}^2}, \qquad St = \frac{fW}{v_{in}}, \tag{1}$$

here, B_{ref} is a reference magnetic field strength, that we will define later. f is the frequency of the long term self-sustained oscillations. Note that N takes the sign of I, thus $N > 0$ for $I > 0$ (which is the oscillation suppressing configuration) and $N < 0$ for $I < 0$ (which is the oscillation enhancing configuration). It should be noted that the Hartmann number $Ha = B_{ref} T (\sigma/\rho\nu)^{1/2} = 0.4$ indicates that no electromagnetic boundary layers are present.

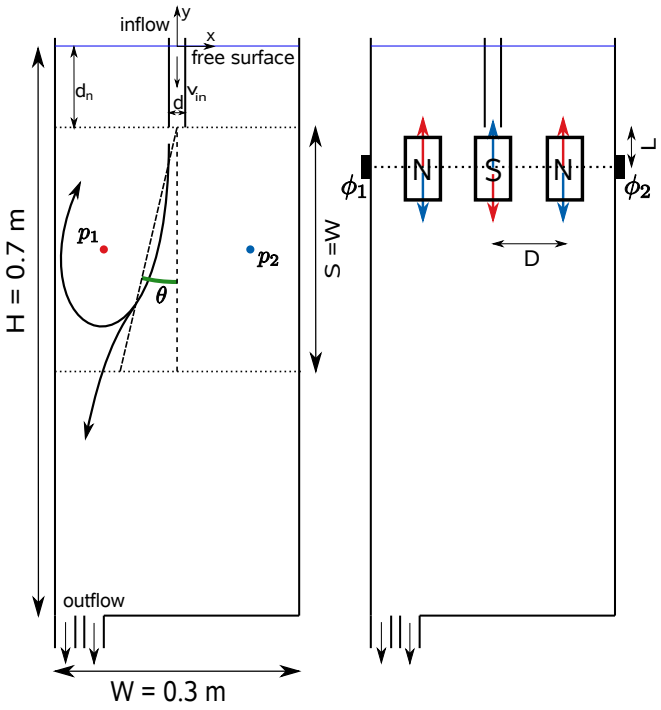

Figure 1: The $z = 0$-plane of the configuration of a single jet in a confined geometry with electromagnetic forcing. The cavity dimension is $H \times W \times T = 0.7 \times 0.3 \times 0.035$ m^3 and a vertically oriented square nozzle with inner diameter $d = 0.01$ m is submerged by $d_n = 0.1$ m below the free liquid surface. (left) The definition of the jet angle θ, defined in between $y = -d_n$ and $y = -d_n - S$ and the monitoring positions p_1 and p_2, located at $(\pm 0.092 \text{ m}, 0.4 \text{ m}, 0 \text{ m})$, are indicated. (right) The locations of the magnets are indicated by rectangles with their respective orientation indicated with either N or S. Electrodes on both sides, indicated with ϕ_1 and ϕ_2, generate a current through the system. The Lorentz forces are indicated by the red arrows for $I < 0$ and by the blue arrows for $I > 0$.

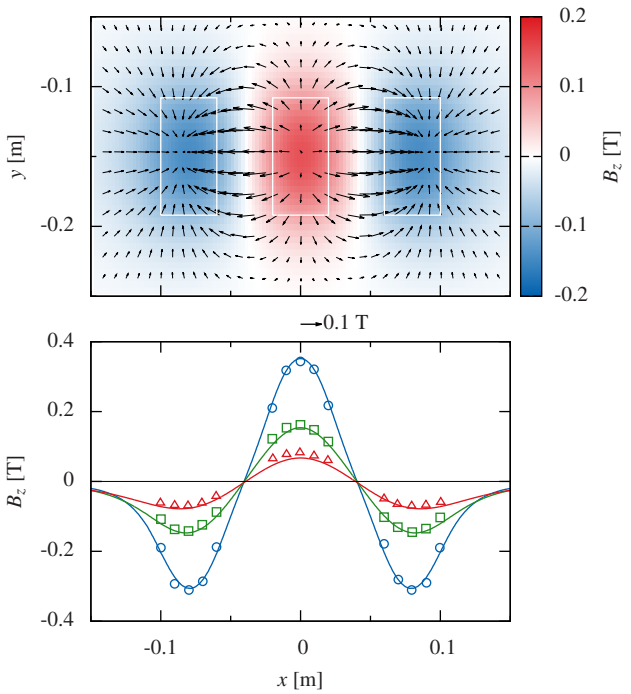

Figure 2: (top) Contours of the z-component of the imposed magnetic field and arrows of x and y components of the magnetic field in the $z = 0$-plane, white rectangles indicate the positions of the three magnets. (bottom) The z-component of the magnetic field for the numerical simulations (solid line) and experiments [6] (symbols) at $y = -0.15$ m for three z-positions in the cavity: close to the back wall ($z/T = -1/2$, blue, circles), in the center of the domain ($z/T = 0$, green, squares) and close to the front wall ($z/T = 1/2$, red, triangles).

2.3. Magnetic field calculation

The imposed magnetic field was modelled based on the z-component of the magnetic field as measured by Kalter et al. [6]. We fit an analytical expression for the magnetic field of block magnets [31] to the reported z-component of the magnetic field, as indicated in Figure 2(bottom). Figure 2(top) shows the computationally imposed magnetic field in the $z = 0$-plane, indicating its three-dimensional character. The reference magnetic field is defined as the magnetic field strength in this plane in the center of the central magnet, thus $B_{ref} = 0.15$ T. The magnitude of the x and y components of the magnetic field in the $z = 0$-plane is of the same order of magnitude as the z component of the magnetic field. The imposed electric current leads to an electric potential as shown in Figure 3(top) and Lorentz forces as shown in Figure 3(bottom) for $I > 0$. For $I < 0$, the electrical potential and consequently the Lorentz force are reversed.

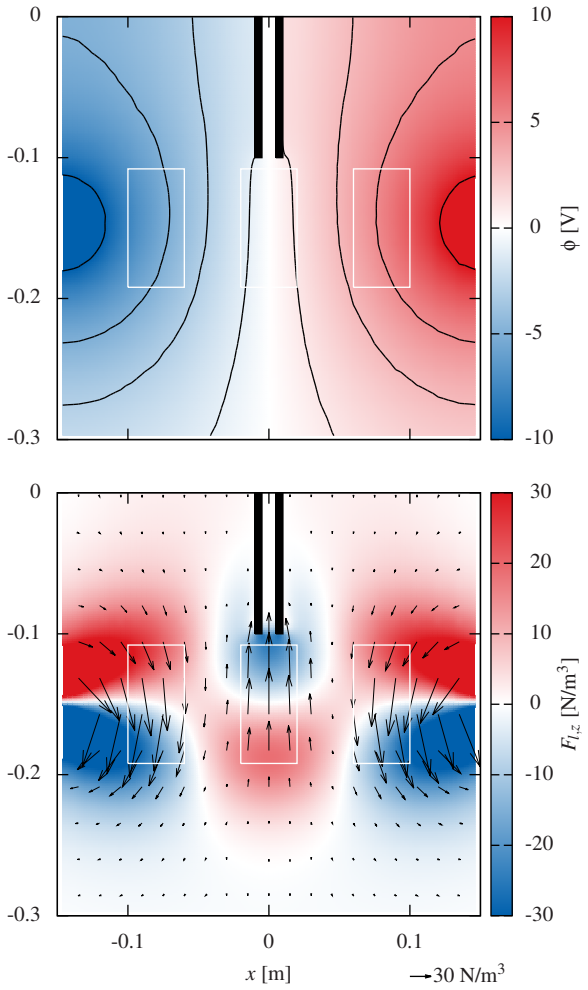

Figure 3: (top) Contours of the electric potential, when a current $I = 4$ A is directed from left to right. (bottom) Contours of the z-component of the corresponding Lorentz force and vectors of the x and y components in the $z = 0$-plane. The position of the magnets is indicated by white rectangles, and the position of the nozzle with black rectangles.

2.4. Flow simulations

The LES filtered, single phase, incompressible Navier-Stokes equations are solved in this study:

$$\begin{aligned} &\frac{\partial v_i}{\partial t} + v_j \frac{\partial v_i}{\partial x_j} \\ &= -\frac{1}{\rho}\frac{\partial p}{\partial x_i} + \frac{\partial}{\partial x_j}\left[(\nu + \nu_{SGS})\left(\frac{\partial v_i}{\partial x_j} + \frac{\partial v_j}{\partial x_i}\right)\right] + f_i. \end{aligned} \tag{2}$$

Here v_i is the velocity, ρ the material density, ν the laminar viscosity, ν_{SGS} the sub-grid-scale viscosity from the LES model, p the pressure and f_i the Lorentz force. The Lorentz force is calculated from the current j_i and magnetic field b_i as [32]

$$f_i = \epsilon_{ijk} j_j b_k \qquad \text{with } j_i = \frac{\sigma}{\rho}\left(-\frac{\partial \phi}{\partial x_i} + \epsilon_{ijk} u_j b_k\right), \tag{3}$$

where σ is the electrical conductivity of the fluid and ϕ is the electric potential, which is obtained from solving the Poisson equation

$$\frac{\partial^2 \phi}{\partial x_i^2} = \frac{\partial}{\partial x_i}\left(\epsilon_{ijk} u_j b_k\right), \tag{4}$$

We use the open source code OpenFOAM 2.1 [33] based on the finite volume method to solve the discretized equations using the PISO scheme.[34] As a sub-grid-scale LES model we use the dynamic Smagorinsky model, which is effective in modelling the subgrid scales in these one-way coupled MHD flows.[35] The domain is discretized in a rectangular, orthogonal grid, consisting of $128 \times 275 \times 34 \approx 1.1 \times 10^6$ grid cells, where the convective and diffusive terms are spatially discretized using a second order central differencing scheme. The time step is dynamically limited to $\max(Co = u\Delta t/\Delta x) = 1$, in a second order fully implicit scheme. More details on the discretization and the wall treatment are given in our previous publication.[23] The contours of the instantaneous ν_{SGS}/ν being smaller than 3 shown in Figure 4(bottom) indicate that this grid resolution is sufficient.

2.5. Validation

The numerical model is validated against experiments [6] for a jet of $Re = 4,700$ and electromagnetic forcing with $N = 0.017$ ($I = 4$ A) in the oscillation suppressing configuration. Figures 4 and 5 show computed time averaged velocities compared to experimental data. The comparisons show a good agreement in the mean velocity between the numerical and experimental results. It is noted that the simulated and measured flow field are not fully symmetric due to the asymmetry in the outflow in the bottom of the domain (see Figure 1). The numerical simulations also show a good agreement in the oscillation frequency for various N, as we show in Figure 9, which also shows the $N - St$ relation obtained from the experiments.

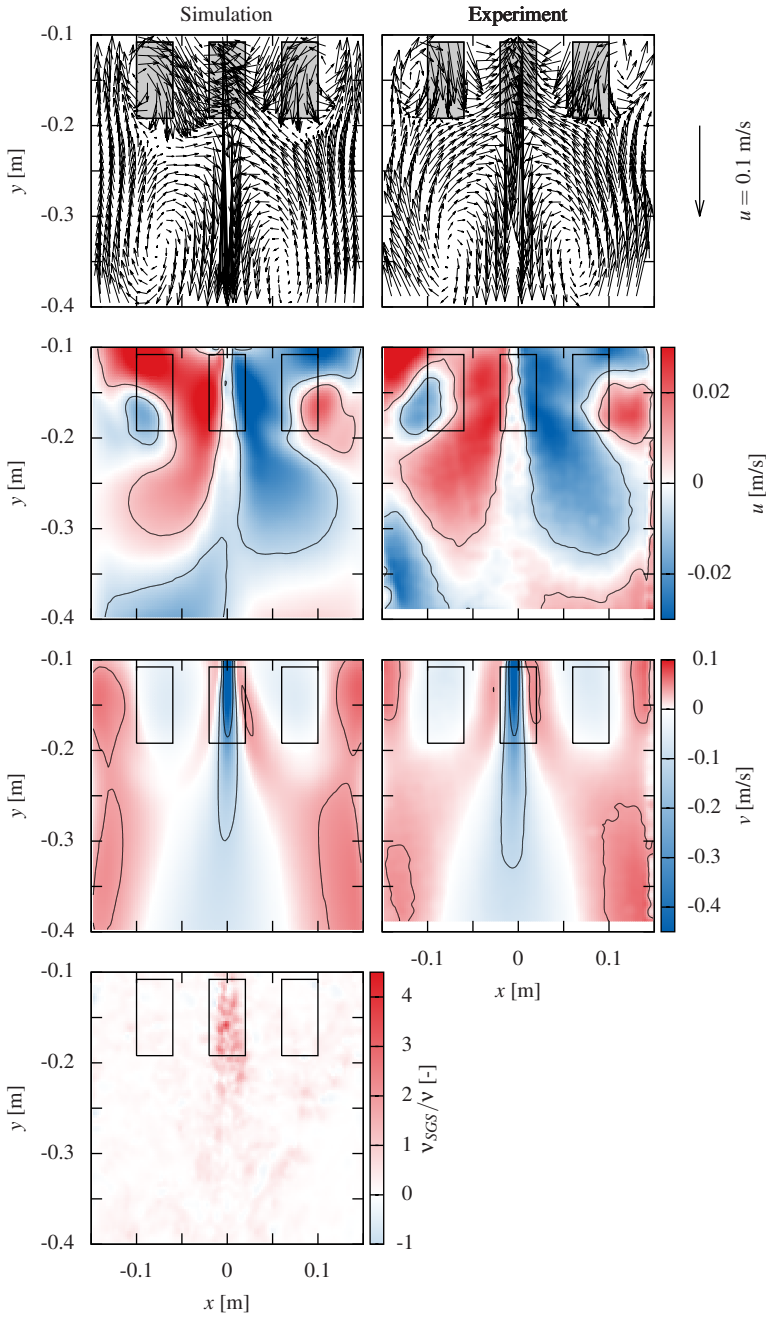

Figure 4: For $Re = 4,700$ and $N = 0.017$ in the $z = 0$-plane, simulation (left) and experiment (right), from top to bottom: Vector fields of the mean velocity, contours of the horizontal mean velocity, contours of the vertical mean velocity and contours of the scaled instantaneous sub-grid-scale viscosity ν_{SGS}/ν. The black rectangles indicate the position of the magnets.

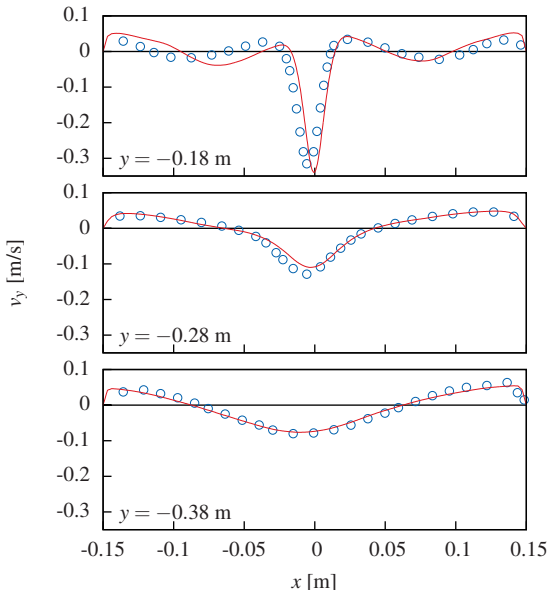

Figure 5: The time averaged vertical velocity component for $y = -0.18$ m, $y = -0.28$ m and $y = -0.38$ m, for $Re = 4,700$ in the oscillation suppressing ($N = 0.017$) configuration for both the numerical simulation (red solid line) and the experiment [6] (symbols).

3. Influence of electromagnetic forcing on self-sustained oscillations

This section described the influence of the electromagnetic force on the mean velocity, oscillation frequency, the pressure difference across the jet, the amplitude of the jet angle oscillation, and the flow regimes.

3.1. Mean velocity

For $Re = 4,700$, we performed numerical simulations for various $-0.075 < N < 0.015$. Figure 6 shows the corresponding mean velocity vector fields, which demonstrates that the velocity field is strongly dependent on N, with the jet and recirculation zone strength increasing for negative N and decreasing for positive N.

The jet velocity, v_{jet}, indicates the strength of the recirculation zone, and its scaling with N can be determined from a vertical momentum balance when considering a control volume of width ΔX centered around the magnet below the jet exit. This control volume is schematically depicted in Figure 7. The average strength of the vertical component of the Lorentz force in this control volume is denoted by F_L. The vertical momentum balance then leads to

$$-\rho d^2 v_{in}^2 + \rho \Delta X T v_{jet}^2 + F_L = 0. \tag{5}$$

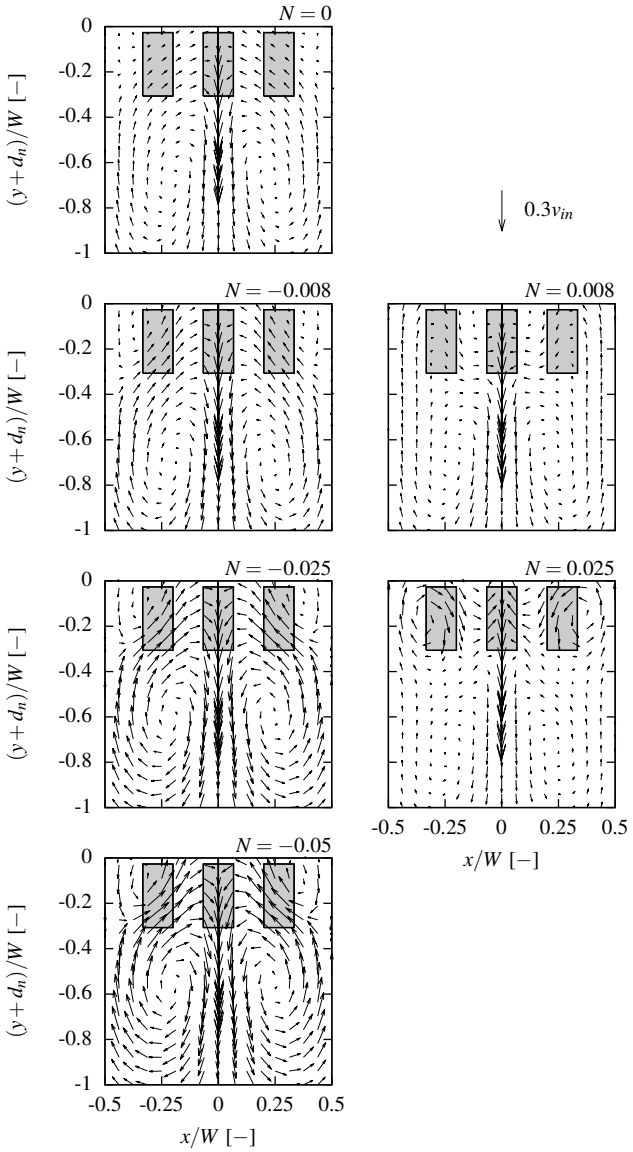

Figure 6: Vector field of the mean velocity for $Re = 4,700$ and Stuart numbers in the range $-0.05 \leq N \leq 0.025$. The positions of the magnets are indicated by gray rectangles.

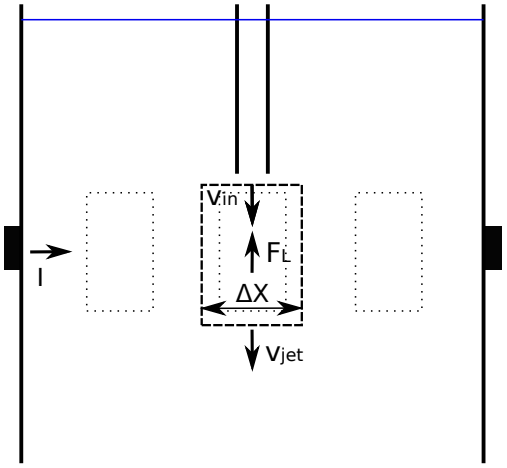

Figure 7: The Lorentz force F_L is active in a control volume of width ΔX, thickness T and certain height. The control volume is used for deriving the scaling relation of v_{jet}/v_{in} as a function of N.

The strength of the Lorentz force scales linearly with the current density (I/area) and the magnetic field strength, hence we know that

$$F_L \propto \frac{IB_{ref}}{\text{area}}. \tag{6}$$

By rearranging Equation 5, using the definition of N (Equation 1) and the above scaling of F_L, we obtain

$$\frac{v_{jet}^2}{v_{in}^2} \propto \frac{d^2}{T\Delta X}\left(1 - cN\right), \tag{7}$$

where c is a positive constant which is solely dependent on geometrical properties of the present configuration. We can now conclude that the square of the velocity in the jet is linearly dependent on N, increasing for $N < 0$ and decreasing for $N > 0$. This is confirmed by our numerical simulations, as shown in Figure 8.

3.2. Oscillation frequency

Without electromagnetic forcing ($N = 0$), it is shown in [6, 23] that the jet oscillates with a constant Strouhal number $St = 0.011$, and thus that $f \sim v_{in} \sim v_{jet}$, for fixed W.

For $N > 0$, the Lorentz force in the jet opposes the inflowing jet, leading to a lower jet velocity. For small, but positive N, the electromagnetic braking is weak, and we confirm that remains $St = 0.011$, as shown in Figure 9. The oscillation frequency does not change until $N > N_{crit}$, when the electromagnetic force becomes dominant over the inertial force and the oscillations are completely suppressed.

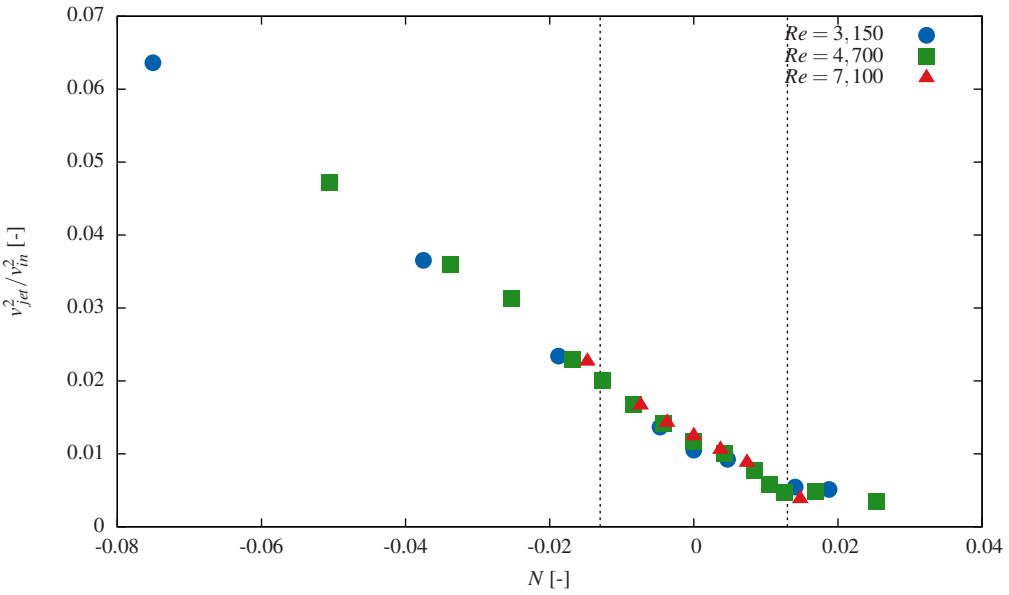

Figure 8: The square of the mean jet velocity (calculated through an area of size $D \times T$ located at $y = -0.19$ m), normalized by the inlet velocity v_{in} as a function of N. The vertical dashed lines indicate $N = \pm N_{crit}$.

For $N < 0$, the Lorentz force is directed in the same direction as the inflowing jet, leading to increased v_{jet} at fixed $_{in}$. From Equation 7 and $f \sim v_{jet}$ it may be expected that for large negative N, $St \propto \sqrt{-N}$. This is indeed observed in the present numerical simulations (see Figure 9) irrespective of Re in the range $3,150 \leq Re \leq 7,100$, showing good agreement with the experimentally observed proportionality of St with $\sqrt{-N}$.[1]

3.3. Pressure oscillations

We define the pressure difference across the jet as $\Delta p = p_2 - p_1$ (see Figure 1). In our earlier paper [23] we have shown that the proportionality of Δp and θ is a key property of the self-sustained jet oscillation.[23] We confirm with Figure 10 that this proportionality remains present for $N \neq 0$. The pressure difference between the center and the edge of a recirculation zone is proportional to the square of the tangential velocity near its edge.[5] As the square of the jet velocity is linearly dependent on N (see Equation 7) we also expect the amplitude of the pressure oscillation, $\langle \Delta p \rangle$, to be linearly dependent on N. This is confirmed by our numerical simulations, as shown Figure 11. This observation is independent of Re.

[1]Please note that in Kalter et al., the definition of the Stuart number and the calculation, are incorrect by a constant factor 3.15. Here, we use the correct values.

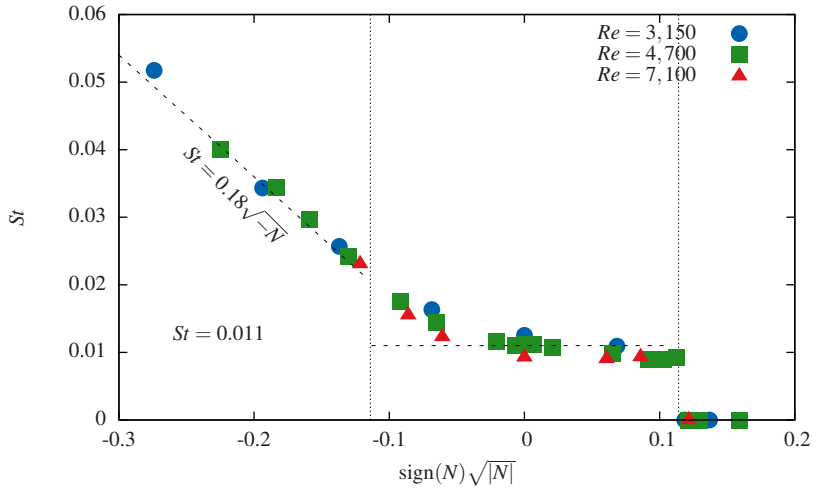

Figure 9: St as a function of N for the oscillation suppressing ($N > 0$) and enhancing ($N < 0$) configuration for $Re = 3,150$ (blue circles), $Re = 4,700$ (green squares) and $Re = 7,100$ (red triangles). The dashed lines indicate the lines $St = 0.011$ and $St = 0.18\sqrt{-N}$ and the vertical lines indicate $N = \pm N_{crit}$.

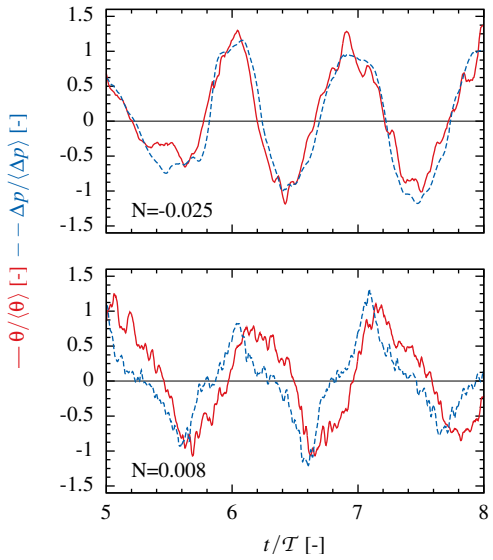

Figure 10: The pressure difference Δp normalized by $\langle \Delta p \rangle$ and the jet angle θ normalized with $\langle \theta \rangle$, as a function of the time normalized with the period $\mathcal{T}$ for $N = -0.025$ (top, $\mathcal{T} = 17$ s, $\langle \Delta p \rangle = 33$ Pa, $\langle \theta \rangle = 26°$) and $N = 0.008$ (bottom, $\mathcal{T} = 52$ s, $\langle \Delta p \rangle = 10$ Pa, $\langle \theta \rangle = 30°$) and $Re = 4,700$.

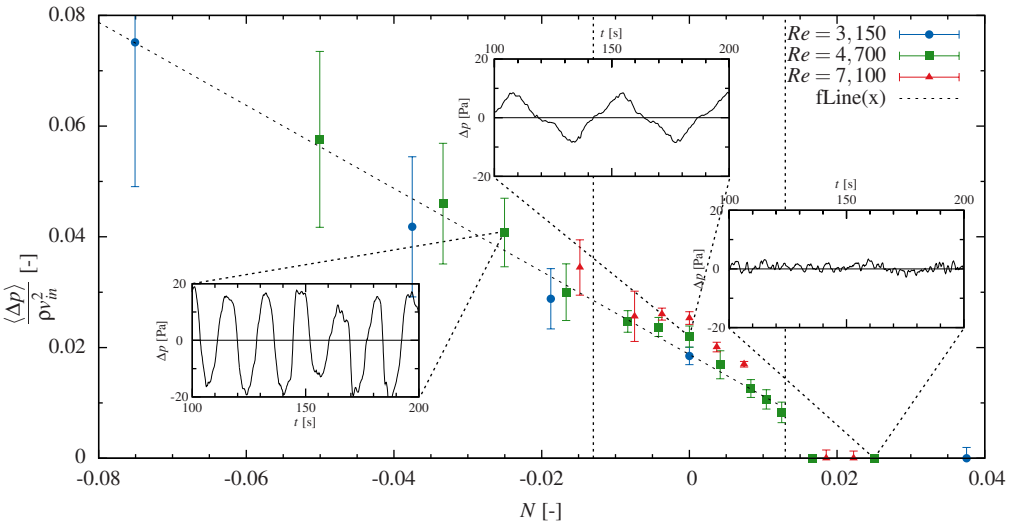

Figure 11: The amplitude $\langle \Delta p \rangle$ of the pressure oscillations, normalized by the energy ρv_{in}^2 as a function of N for $Re = 3,150$ (blue circles), $Re = 4,700$ (green squares) and $Re = 7,100$ (red triangles). The insets show the instantaneous Δp for $N = -0.025$, $N = 0$ and $N = 0.025$. The vertical dashed lines indicate $\pm N_{crit}$. The error bars indicate the standard deviation of the calculated $\langle \Delta p \rangle$.

3.4. Jet angle amplitude

The amplitude of the jet angle oscillation, $\langle \theta \rangle$, is also dependent on N, as we show in Figure 12. For $N = 0$, $\langle \theta \rangle$ is the largest ($\langle \theta \rangle = 18°$), and can be obtained from geometrical considerations.[23]

In the oscillation suppressing configuration ($N > 0$), the oscillations vanish for $N > N_{crit}$, whereas in the oscillation enhancing configuration ($N < 0$), $\langle \theta \rangle$ reaches a constant value, i.e, $\langle \theta \rangle = 12.5^{\circ}$ for $N < -N_{crit}$. For $|N| < N_{crit}$, $\langle \theta \rangle$ roughly diminishes quadratically with N, i.e.:

$$\langle \theta \rangle = \theta_{max} - \beta \left(\frac{N}{N_{crit}} \right)^2, \tag{8}$$

with $\theta_{max} = 18°$ and $\beta = 5.5°$. We determined $N_{crit} = 0.013$. Both functions for $\langle \theta \rangle$ are indicated in Figure 12.

The physical reasoning behind this behavior of $\langle \theta \rangle$ becomes apparent from Figure 6. In the oscillation suppressing configuration ($N > 0$), the flow is pushed downward by the magnets in the corners. This prevents the growth of the recirculation zones and hence limits $\langle \theta \rangle$. Conversely, in the oscillation enhancing configuration ($N < 0$), the recirculation zone gets elongated (see Figure 6 for $N = -0.008$), which also leads to a reduced jet angle. Increasing the current further ($N < -N_{crit}$), leads to the flow mainly being driven by the electromagnetic forcing, a approximately constant flow profile and hence constant $\langle \theta \rangle$.

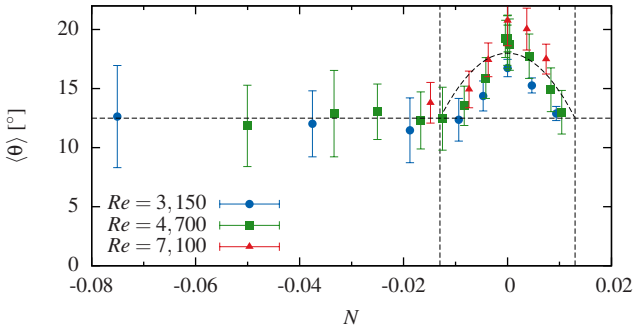

Figure 12: The amplitude $\langle\theta\rangle$ of the jet angle oscillation as a function of N, with $\langle\theta\rangle = \theta_{max} - \beta(N/N_{crit})^2$ with $\theta_{max} = 18°$ and $\beta = 5.5°$, for $|N| < N_{crit} = 0.013$. $\langle\theta\rangle = 12.5°$ for $N < -N_{crit}$, and $\langle\theta\rangle = 0$ for $N > N_{crit}$.

3.5. Flow regimes

We can now conclude that for varying N, three regimes can be distinguished, independent of Re and separated by $N_{crit} = 0.013$:

- For $N > N_{crit}$, oscillations are suppressed.
- For $-N_{crit} < N < N_{crit}$, self-sustained oscillations by the jet are dominant. St remains constant and has the same value as for $N = 0$. However, the jet amplitude decreases quadratically with $|N|$.
- For $N < -N_{crit}$, the Lorentz forces are dominant and control the oscillations in the domain.

4. Zero-dimensional model of the jet oscillation

In this section, we describe a zero-dimensional DDE-type model, which quantitatively describes single jet oscillations, then we show how it can be applied to electromagnetically forced single jet oscillations. Such a quantitative description can be used to predict the frequency and waveform of jet oscillations, and is an alternative for experiments of full three-dimensional numerical simulations.

4.1. Unforced flow ($N = 0$)

As we have shown earlier, the self-sustained oscillation of the jet, in the absence of electromagnetic forcing, can be explained from the transient behaviour of Δp and θ. [23] When the jet is slightly oriented to one side (say, the right, $\theta < 0$), the recirculation zone on the right will be stronger, i.e., it has a smaller diameter and higher velocities. This leads to a larger pressure deficit in the recirculation zone, deflecting the jet even further. The jet angle will subsequently reach an extreme, as the jet impinges on the side wall and the recirculation zone can not shrink any further. Subsequently, the fluid escapes the strong recirculation zone on the right and feeds the recirculation zone on the left. The pressure

deficit in the recirculation zone on the right diminishes, and the jet angle will deflect to the left.

In [23] we showed, from a horizontal momentum balance, that the growth of the jet angle during the initial stage of the oscillation is proportional to the horizontal pressure difference over the jet

$$\frac{d\theta}{dt} \propto \Delta p \tag{9}$$

Furthermore, we have shown that $\Delta p \sim \theta$, and hence

$$\frac{d\theta}{dt} = r\theta, \tag{10}$$

where r is the growth rate of the oscillation.

The maximum jet angle, $\langle\theta\rangle$, that can be reached is constrained by the geometry. This acts as a damping term on the oscillation, hence

$$\frac{d\theta}{dt} = \left(r - \mu\theta^2\right)\theta, \tag{11}$$

where μ is the obstruction parameter, related to $\langle\theta\rangle$.

In the last stage of the oscillation, the strong recirculation quickly decays in a timescale τ, which is of the order of the turnover time of the recirculation zone. This leads to the full model equation [23]

$$\frac{d}{dt}\theta(t) = r\theta(t) - \mu\theta^3(t) - k\theta(t-\tau), \tag{12}$$

where k is the decay rate for the destruction of the strong recirculation zone. Equation 12 is a zero-dimensional model, which is of the Delay Differential Equation (DDE) type. Its model constants can be determined *a priori* as a function of inflow parameters and geometry only. [23]

4.2. Electromagnetically forced flow ($N \neq 0$)

Here we argue that the general shape of model equation 12 remains valid for $N \neq 0$, but with modified model parameters that will now also depend on N. We will discuss the influence of $N \neq 0$ on each of the three right-hand terms in Equation 12, viz. (i) the growth term, (ii) the damping term, and (iii) the delayed decay term.

(i) Equation 9 remains true for $N \neq 0$ as the imposed Lorentz force in the present configuration is dominantly vertical (see Figure 3). Furthermore, from Figure 10 we conclude that Δp and θ remain proportional. Therefore, Equation 10 remains valid as well for $N \neq 0$. Thus, the form of the growth term in Equation 12 remains unchanged. The constant of proportionality, the growth rate r, is however influenced by the Lorentz force, as Δp is highly dependent on the electromagnetic forcing. We have shown in Figure 11 that $\langle\Delta p\rangle$ depends linearly on N. Due to this dependence, we also expect r to be linearly dependent on N.

(ii) For each value of N, we find a specific value for the maximum jet deflection angle $\langle\theta\rangle$. For $N = 0$, only the geometry obstructs the motion of the jet angle, leading to $\langle\theta\rangle = 18°$. [23] In Figure 12 above, we have shown that the maximum jet angle depends quadratically on N for $|N| < N_{crit}$. For $N > N_{crit}$ the oscillations vanish, and thus $\langle\theta\rangle = 0$, whereas for $N < -N_{crit}$, we have shown that the oscillation is enhanced mainly by the electromagnetic forcing and the maximum jet angle is constant, $\langle\theta\rangle = 12.5^{\circ}$. For each N, the maximum jet deflection can be accounted for through a damping term of the form of the second right-hand term in Equation 12, with the model constant μ now being a function of N.

(iii) Since, for $|N| < N_{crit}$ the flow is dominated by inertial forces, the description of the oscillation by means of the delayed feedback mechanism [23] still holds, with the model constant being slightly dependent on N.

For $N < -N_{crit}$, the electromagnetic forcing has a larger influence on the delay time. The velocities in the domain quickly increase with decreasing N, leading to a shorter delay time τ and larger influence of the feedback induced destruction of the recirculation zone pressure minimum. We therefore expect both model constants k and τ in the delayed decay term to strongly depend on N for $N < -N_{crit}$.

5. Determination of the model parameters and its implications

For $N = 0$, the self-sustained jet oscillations in a thin, confined cavity can be described by Equation 12, which contains four model parameters, r, μ, k and τ. These parameters can be determined *a priori* based on Re, W/d, v_{in} and W.[23] In this section we will demonstrate that the electromagnetic forcing can be incorporated with one additional parameter, viz. N.

5.1. Non-dimensional model

Model Equation 12 can be written in terms of the dimensionless time $t' = rt$ and jet angle $\theta' = \sqrt{\mu/r}\theta$: [23]

$$\frac{d\theta'}{dt'} = \theta' - \theta'^3 - \alpha\theta' \left(t' - \delta\right). \tag{13}$$

The variables $\alpha = k/r$ and $\delta = r\tau$ denote the relative strength of the feedback mechanism compared to the growth rate and the dimensionless delay time respectively. The neutral curve, obtained from a linear stability analysis, is [36, 23]

$$\delta_n(\alpha) = \arccos\left(\frac{3\alpha - 2}{\alpha}\right)\left(\alpha^2 - (3\alpha - 2)^2\right)^{-\frac{1}{2}}. \tag{14}$$

This critical curve separates the stable and oscillatory regimes of the model Equation 13. For $\delta < \delta_n(\alpha)$, all modes are stable and no oscillations will be present. For $\delta > \delta_n(\alpha)$, oscillatory modes will be sinusoidal of shape close to the neutral curve and approach block-waves for $\delta \geq 10$.

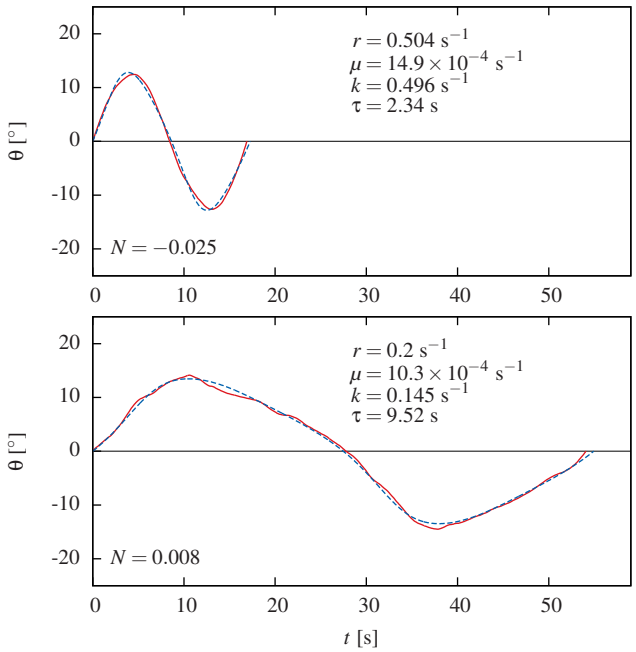

Figure 13: The phase averaged jet angle amplitude (solid red line) in conjunction with the model fit (dashed blue line), for $Re = 4,700$ and for $N = -0.025$ (top) and $N = 0.008$ (bottom).

5.2. Parameter fitting

From our numerical simulations for varying N, we calculate $\theta(t)$ and the phase average jet angle amplitude. From a fitting procedure we determine the best fitting parameter set r, μ, k, τ following the method outlined in.[23]

In Figure 13 we show the phase averaged jet angle amplitude together with the solution of the DDE model for the fitted parameter set, for both $N = -0.025$ and $N = 0.008$. This figure shows the good agreement between the zero-dimensional model solution and the actual jet angle profile obtained from the LES simulations.

For $N > N_{crit}$ no oscillations are present, hence we cannot calculate a phase average, nor determine α and δ from the numerical simulations. However, for $N < N_{crit} = 0.013$ we determine the parameters α and δ for $-5N_{crit} \leq N \leq N_{crit}$, $3,150 \leq Re \leq 7,100$ and $W/d = 30$.

We show the fitted parameters α and δ for this parameter set and the neutral curve δ_n (Equation 14) in Figure 14. From this stability diagram a clear distinction between the inertial dominated and electromagnetically dominated regimes becomes apparent. For $|N| < N_{crit}$ the jet oscillation itself is dominant, and we showed in our previous publication [23], that the parameters describing these oscillation are close to the neutral curve. And indeed, this is observed in Figure

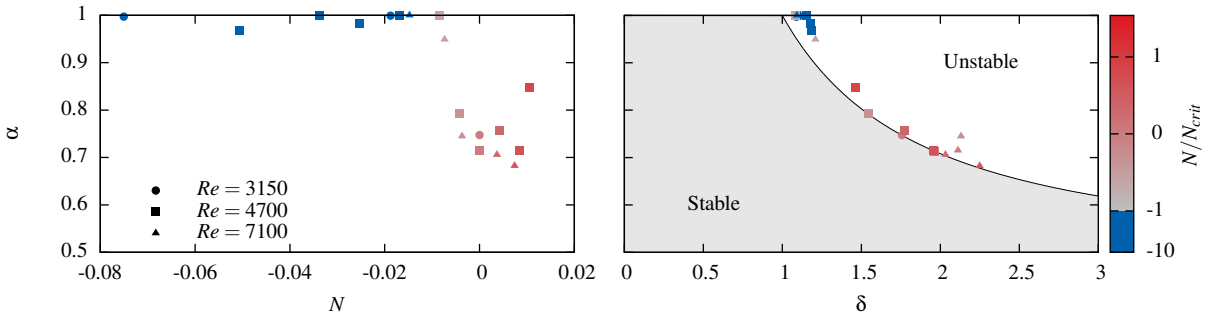

Figure 14: For $-0.08 \leq N \leq 0.02$ (color of symbols) and $3,150 \leq Re \leq 7,100$ (symbol type) (left) α as a function of N and (right) the neutral curve (Equation 14, solid line), with the shaded and non-shaded area denoting the regions of stable and oscillatory modes, respectively. The parameter values (δ, α) are indicated in the diagram, where the colors indicate $|N| < N_{crit}$ (grey-red) and $N < -N_{crit}$ (blue) as well.

14. For $N < -N_{crit}$, the parameters cluster together close to $(\delta, \alpha) = (1, 1)$. In other words, for $N < -N_{crit}$ the normalized behavior of the system does not change. Although the parameters α and δ sparsely change over a variation in N, the underlying variables r, μ, k and τ, will change significantly as we will later show.

5.3. Parameter estimation

In [23], from a fitting approach to LES simulations, it was found that in the absence of electromagnetic forcing the model parameters r and τ are given by

$$r = \kappa_1 \frac{v_{in}}{W} Re^{-\frac{1}{4}} \left(\frac{W}{d}\right)^{-\frac{1}{2}}, \qquad \tau = \kappa_2 \frac{W}{v_{in}} Re^{\frac{5}{9}}, \tag{15}$$

with $\kappa_1 = 5.9$ and $\kappa_2 = 0.13$.

In Section 4.2 we anticipated that r decreases linearly with N. For $N = 0$, the present model should reduce to the unforced model, hence we may pose

$$\kappa_1(N) = \kappa_1 \left(1 - \lambda_1 \frac{N}{N_{crit}}\right), \tag{16}$$

which thus consists of a contribution by the inertial force and a contribution by the magnetic force. From our numerical simulations and fitted model parameters, we determine that $\lambda_1 = 0.49 \pm 0.02$.

For the delay time τ such a unified approach across both the inertially dominated and electromagnetically dominated regimes is not possible. For $-N_{crit} < N < 0$ we expect a smaller delay time, since fluid is accelerated in the recirculation zone, and for $0 < N < N_{crit}$ the fluid is decelerated and we expect the delay time to increase. Hence, for $|N| < N_{crit}$

$$\kappa_2(N) = \kappa_2 \left(1 + \lambda_2 \frac{N}{N_{crit}}\right). \tag{17}$$

From our numerical simulations and fitted parameters we find that $\lambda_2 = 0.58 \pm 0.09$.

For $N < -N_{crit}$ we use the above observation that δ remains close to constant, and hence we define

$$\tau = \frac{\delta_{min}}{r}, \tag{18}$$

with $\delta_{min} = 1.13$ the average value for δ observed in our simulations. Hence, with r from Equations 15 and 16, τ can be determined.

For given N we now determine k from r, τ and δ. For $|N| < N_{crit}$, the pair (α, δ) resides close to the neutral curve $\delta_n(\alpha)$ (Equation 14), which thus determines α. For $N < -N_{crit}$, we use the above observation from Figure 14 that $\alpha \approx 0.99$. From α we determine $k = \alpha r$.

μ follows from the amplitude $\langle \theta' \rangle$ of the dimensionless form of the DDE model equation (Equation 13) [23] and the behavior of $\langle \theta \rangle$. For $N = 0$ we found $\langle \theta' \rangle = \sqrt{2\left(1 - \alpha^2\right)}$. This also holds for $|N| < N_{crit}$. For $N < -N_{crit}$, the parameters are no longer distributed along the neutral curve, but given by $\alpha \approx 0.99$ and $\delta = 1.13$ above. For this regime we find $\langle \theta' \rangle = \gamma = 0.61$.

$$\mu = \begin{cases} \dfrac{2r\left(1 - \alpha^2\right)}{\langle \theta \rangle^2} & \text{if } |N| < N_{crit} \\ \dfrac{\gamma^2 r}{\langle \theta \rangle^2} & \text{if } N < -N_{crit} \end{cases}, \tag{19}$$

Now, for given N, the model parameters r, μ, k and τ can be determined from Equations 15 and 16, Equation 19, $k = \alpha r$ and Equations 15, 17 and 18, respectively

5.4. Model application

Figure 15 compares the parameters obtained from the model presented in Equations 15-19 with the parameters obtained from the fit of the phased-average jet oscillation profiles from the numerical simulations. With this figure we confirm that the present model gives the correct model parameters to determine the jet oscillation properties.

In table 1 we compare the frequencies obtained from the LES simulations and the presented zero-dimensional model. The table demonstrates that our model correctly predicts the single jet oscillation frequency along the range $-6N_{crit} \leq N \leq N_{crit}$, as is also indicated with Figure 16. The deviation is only larger than 10% for the most extreme cases ($N = N_{crit}$ and $N = -6N_{crit}$), where the first is close to being damped and the latter enhanced, to such an extend that the oscillations become irregular.

In Figure 17 we show the numerically obtained jet angle profile and the jet angle profile obtained from the model for several combinations of Re and N. The figure demonstrates that the zero-dimensional DDE-type model can successfully be applied on the electromagnetic forcing of a self-sustained oscillating jet, both in the inertia, as in the electromagnetic force dominant regimes. For larger negative N ($N = -0.075$, bottom right in figure 17), the forced flow shows

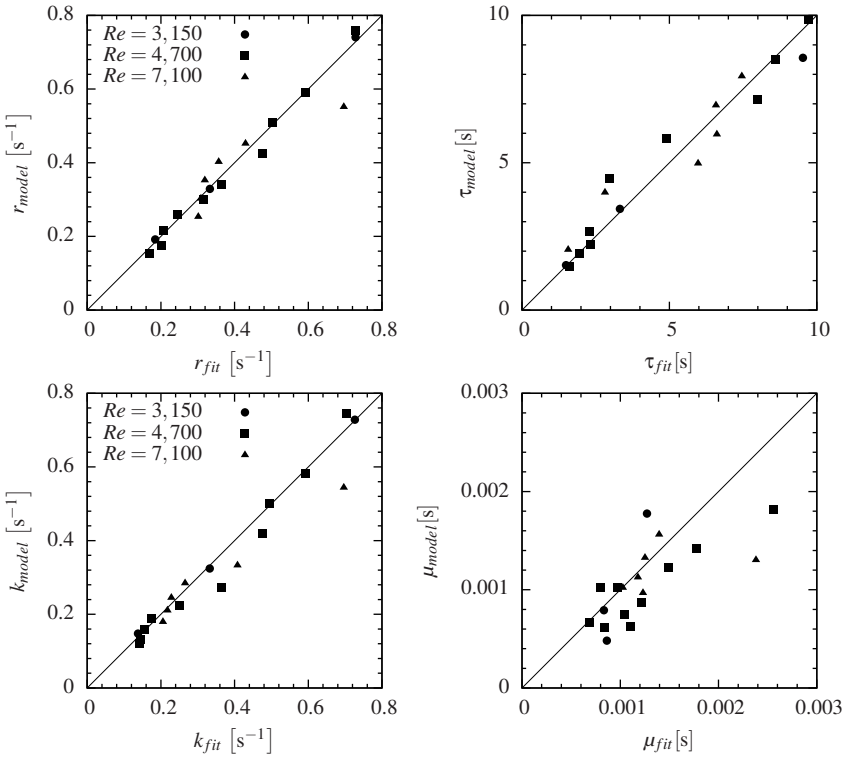

Figure 15: Parity plot for r (top left), τ (top right), k (bottom left) and μ (bottom right) showing the fitted parameter value (horizontal axis) compared to the parameter value obtained from the model (Equations 15-19).

irregular behavior, which is observed from the significant variation in period and amplitude during the oscillation. This phenomenon due to the strong amplification of the oscillation for large negative N is not described by the present model. For the other N however, the presented model shows a good agreement in profile shape and frequency.

6. Conclusion

We studied the effect of an electromagnetic body force on self-sustained jet oscillations in a confined cavity. Three flow regimes can be distinguished, that are separated by the critical Stuart number N_{crit}: 1) for $N > N_{crit}$, all inertia induced large scale oscillations are suppressed by electromagnetic body forces, 2) for $|N| < N_{crit}$, the jet inertia is dominant compared to the electromagnetic force, but the latter influences the jet oscillation in amplitude and frequency, 3) for $N < -N_{crit}$, the electromagnetic forces dominate the flow and control the flow oscillations. For the configuration studied in this paper we found $N_{crit} =$

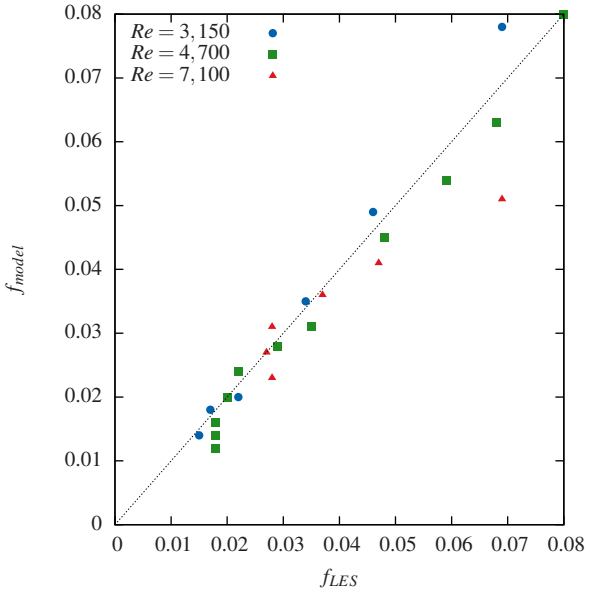

Figure 16: Parity plot for the frequency showing the oscillation frequency obtained from the numerical simulations (horizontal axis) compared to the oscillation frequency obtained from the zero-dimensional model (vertical axis).

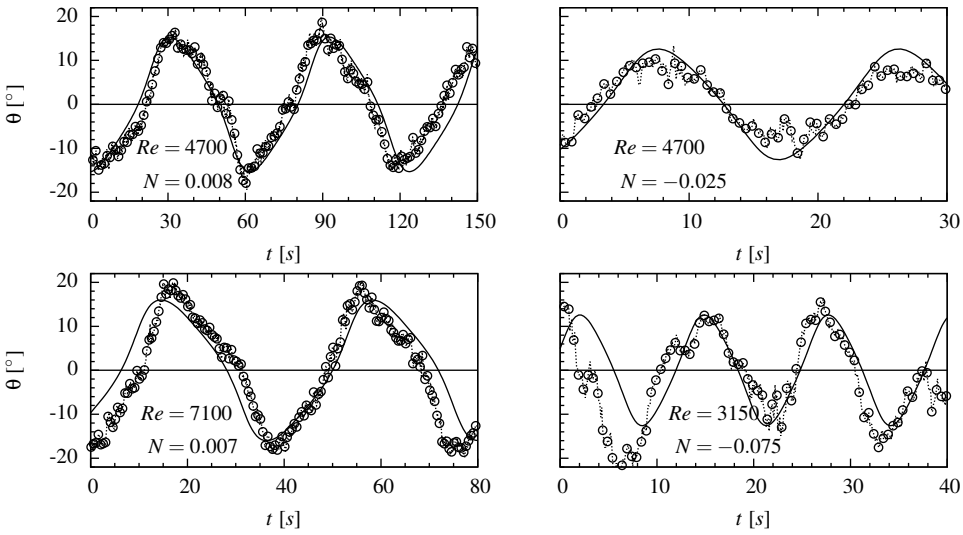

Figure 17: Example model solution (solid line) and the numerical solution (symbols and dashed line) for several combinations of Re and N, as indicated in the graphs.

Table 1: This table compares the oscillation frequency obtained from the LES simulations and the zero-dimensional model equation as a function of Re and N.

Re	N	f_{LES} [Hz]	f_{model} [Hz]
3150	−0.075	0.069	0.078
3150	−0.038	0.046	0.049
3150	−0.019	0.034	0.035
3150	−0.005	0.022	0.020
3150	0	0.017	0.018
3150	0.005	0.015	0.014
3150	0.014	–	–
4700	−0.051	0.080	0.080
4700	−0.034	0.068	0.063
4700	−0.026	0.059	0.054
4700	−0.017	0.048	0.045
4700	−0.009	0.035	0.031
4700	−0.004	0.029	0.028
4700	0	0.022	0.024
4700	0.004	0.020	0.020
4700	0.009	0.018	0.016
4700	0.011	0.018	0.014
4700	0.013	0.018	0.012
4700	0.015	–	–
7100	−0.015	0.069	0.051
7100	−0.007	0.047	0.041
7100	−0.004	0.037	0.036
7100	0.0	0.028	0.031
7100	0.004	0.027	0.027
7100	0.007	0.028	0.023

0.013.

We incorporated the effect of the electromagnetic forcing in a zero-dimensional DDE-type model that describes the jet oscillation. The additional Lorentz force is included in the model by the additional dependence on N. We have shown that this newly defined model correctly represents the jet oscillation for the Reynolds number $3150 \leq Re \leq 7100$ and $-6N_{crit} \leq N \leq N_{crit}$.

Although this paper only addresses a specific configuration of electromagnetic forcing, we believe that the method can also be applied on different EMBr configurations and even different types of body forces. This means that one can expect to find three regimes, a jet inertia dominated regime, an oscillation enhancing regime and an oscillation suppressing regime. The effect of these forces on the zero-dimensional model for the jet oscillation will be dependent on a dimensionless number describing the ratio of the imposed force and the inertial force.

For large negative N the oscillations are more irregular with respect to the deviation in the amplitude between periods. The currently presented model does not include this irregularity in the oscillation.

The forced single jet oscillation model also has potential for other types of forced single jet flows, such as jets with a different density, or by application of acoustic forcing. [37, 38, 39, 40, 41]

7. Acknowledgments

This work was supported by the Dutch Technology Foundation STW, Tata Steel and ABB. We thank SURFsara for the support in using the Lisa Compute Cluster, project code MP-235-12. Furthermore, we thank Jasper Hollander for his assistance in the initial set-up of the numerical simulations.

[1] S. Garcia-Hernandez, R. Morales, J. De Jess Barreto, K. Morales-Higa, Numerical optimization of nozzle ports to improve the fluidynamics by controlling backflow in a continuous casting slab mold, ISIJ International 53 (10) (2013) 1794–1802.

[2] H. Arcos-Gutierrez, G. Barrera-Cardiel, J. d. J. Barreto, S. Garcia-Hernandez, Numerical Study of Internal SEN Design Effects on Jet Oscillations in a Funnel Thin Slab Caster, ISIJ International 54 (6) (2014) 1304–1313.

[3] X. Peng, J. Zhou, Y. Qin, Improvement of the temperature distribution in continuous casting moulds through the rearrangement of the cooling water slots, Journal of Materials Processing Technology 167 (2-3) (2005) 508–514.

[4] L. Zhang, Y.-M. Rong, H.-F. Shen, T.-Y. Huang, Solidification modeling in continuous casting by finite point method, Journal of Materials Processing Technology 192-193 (2007) 511–517.

[5] R. Kalter, M. Tummers, S. Kenjereš, B. Righolt, C. Kleijn, Oscillations of the fluid flow and the free surface in a cavity with a submerged bifurcated nozzle, International Journal of Heat and Fluid Flow 44 (2013) 365–374.

[6] R. Kalter, M. J. Tummers, S. Kenjereš, B. W. Righolt, C. R. Kleijn, Effects of electromagnetic forcing on self-sustained jet oscillations, Physics of Fluids 26 (6) (2014) 065101.

[7] R. Kalter, B. W. Righolt, S. Kenjereš, C. R. Kleijn, M. J. Tummers, Experimental Modeling of Heat Transfer in a Continuous Casting Mould Model, ASME, V01CT16A005, 2014.

[8] M. Y. Ha, H. G. Lee, S. H. Seong, Numerical simulation of three-dimensional flow, heat transfer, and solidification of steel in continuous casting mold with electromagnetic brake, Journal of Materials Processing Technology 133 (3) (2003) 322–339.

[9] Y. Haiqi, W. Baofeng, L. Huiqin, L. Jianchao, Influence of electromagnetic brake on flow field of liquid steel in the slab continuous casting mold, Journal of Materials Processing Technology 202 (1-3) (2008) 179–187.

[10] R. Kalter, M. J. Tummers, S. Kenjereš, B. W. Righolt, C. R. Kleijn, Electromagnetic flow control of a bifurcated jet in a rectangular cavity, International Journal of Heat and Fluid Flow 47 (2014) 113–122.

[11] S. Kenjereš, Electromagnetic enhancement of turbulent heat transfer, Physical Review E 78 (6) (2008) 066309.

[12] S. Kenjereš, Large eddy simulations of targeted electromagnetic control of buoyancy-driven turbulent flow in a slender enclosure, Theor. Comput. Fluid Dyn. 23 (6) (2009) 471–489, ISSN 0935-4964, 1432-2250.

[13] L. Rossi, J.-P. Thibault, Investigation of wall normal electromagnetic actuator for seawater flow control, Journal of Turbulence 3 (2002) N5.

[14] K. Breuer, J. Park, C. Henoch, Actuation and control of a turbulent channel flow using Lorentz forces, Physics of Fluids 16 (4) (2004) 897–907.

[15] J. Pang, K.-S. Choi, Turbulent drag reduction by Lorentz force oscillation, Physics of Fluids 16 (5) (2004) L35–L38, ISSN 1070-6631.

[16] V. Shatrov, G. Gerbeth, Electromagnetic flow control leading to a strong drag reduction of a sphere, Fluid Dynamics Research 36 (3) (2005) 153.

[17] V. Shatrov, G. Gerbeth, Magnetohydrodynamic drag reduction and its efficiency, Physics of Fluids 19 (3).

[18] C. Henoch, J. Stace, Experimental investigation of a salt water turbulent boundary layer modified by an applied streamwise magnetohydrodynamic body force, Physics of Fluids 7 (6) (1995) 1371–1383.

[19] C. Lee, J. Kim, Control of the viscous sublayer for drag reduction, Physics of Fluids 14 (7) (2002) 2523–2529.

[20] T. Weier, G. Gerbeth, G. Mutschke, O. Lielausis, G. Lammers, Control of Flow Separation Using Electromagnetic Forces, Flow, Turbulence and Combustion 71 (1) (2003) 5–17.

[21] S. Dattarajan, H. Johari, Control of a separating boundary layer with Lorentz force actuators, Physics of Fluids 20 (4).

[22] T. Honeyands, J. Herbertson, Flow dynamics in thin slab caster moulds, Steel Research International 66 (7) (1995) 287–293.

[23] B. W. Righolt, S. Kenjereš, R. Kalter, M. J. Tummers, C. R. Kleijn, Dynamics of an oscillating turbulent jet in a confined cavity, Physics of Fluids 27 (2015) 095107, doi:10.1063/1.4930926.

[24] G. Bouchet, E. Climent, Unsteady behavior of a confined jet in a cavity at moderate Reynolds numbers, Fluid Dynamics Research 44 (2) (2012) 025505, ISSN 1873-7005.

[25] E. Villermaux, E. Hopfinger, Self-sustained oscillations of a confined jet: a case study for the non-linear delayed saturation model, Physica D: Nonlinear Phenomena 72 (3) (1994) 230–243, ISSN 0167-2789.

[26] A. Maurel, P. Ern, B. J. A. Zielinska, J. E. Wesfreid, Experimental study of self-sustained oscillations in a confined jet, Physical Review E 54 (4) (1996) 3643–3651.

[27] T. Kolšek, N. Jelić, J. Duhovnik, Numerical study of flow asymmetry and self-sustained jet oscillations in geometrically symmetric cavities, Applied Mathematical Modelling 31 (10) (2007) 2355–2373.

[28] N. A. Molloy, P. L. Taylor, Oscillatory Flow of a Jet into a Blind Cavity, Nature 224 (5225) (1969) 1192–1194.

[29] N. Lawson, M. Davidson, Self-Sustained Oscillation of a Submerged Jet in a Thin Rectangular Cavity, Journal of Fluids and Structures 15 (1) (2001) 59–81, ISSN 0889-9746.

[30] A. Mataoui, R. Schiestel, Unsteady phenomena of an oscillating turbulent jet flow inside a cavity: Effect of aspect ratio, Journal of Fluids and Structures 25 (1) (2009) 60–79, ISSN 0889-9746.

[31] E. V. Votyakov, E. Zienicke, Y. B. Kolesnikov, Constrained Flow Around a Magnetic Obstacle, Journal of Fluid Mechanics 610 (2008) 131–156.

[32] S. Kenjereš, K. Hanjalić, On the implementation of effects of Lorentz force in turbulence closure models, International Journal of Heat and Fluid Flow 21 (3) (2000) 329–337.

[33] H. G. Weller, G. Tabor, H. Jasak, C. Fureby, A tensorial approach to computational continuum mechanics using object-oriented techniques, Computers in Physics 12 (6) (1998) 620–631, ISSN 0894-1866.

[34] R. I. Issa, Solution of the implicitly discretised fluid flow equations by operator-splitting, Journal of Computational Physics 62 (1) (1986) 40–65, ISSN 0021-9991, doi:10.1016/0021-9991(86)90099-9.

[35] B. Knaepen, P. Moin, Large-eddy simulation of conductive flows at low magnetic Reynolds number, Physics of Fluids 16 (5) (2004) 1255.

[36] M. Suarez, P. Schopf, A delayed action oscillator for ENSO, Journal of the Atmospheric Sciences 45 (21) (1988) 3283–3287.

[37] P. A. Monkewitz, D. W. Bechert, B. Barsikow, B. Lehmann, Self-excited oscillations and mixing in a heated round jet, Journal of Fluid Mechanics 213 (1990) 611–639.

[38] M. Yu, T. Lin, Y. Hsieh, Influence of acoustic forcing on the near field development of a heated plane jet, Experimental Thermal and Fluid Science 25 (1-2) (2001) 13–22.

[39] C. Zhang, S. Eckert, G. Gerbeth, The Flow Structure of a Bubble-Driven Liquid-Metal Jet in a Horizontal Magnetic Field, Journal of Fluid Mechanics 575 (2007) 57–82.

[40] M. Juniper, L. Li, J. Nichols, Forcing of self-excited round jet diffusion flames, Proceedings of the Combustion Institute 32 I (2009) 1191–1198.

[41] S. Voropayev, C. Nath, H. Fernando, Mixing by turbulent buoyant jets in slender containers, Physics Letters, Section A: General, Atomic and Solid State Physics 376 (45) (2012) 3213–3218.

Appendix A. Electromagnetic field

The analytical expression for the imposed magnetic field, is based on the algebraic calculations by Votyakov et al.:

$$B_x(x,y,z) = \frac{1}{B_0}\sum_{k=\pm1}\sum_{j=\pm1}\sum_{i=\pm1}(ijk)\,\mathrm{arctanh}\left[\frac{y-jM_y}{r(i,j,k)}\right], \tag{A.1}$$

$$B_y(x,y,z) = \frac{1}{B_0}\sum_{k=\pm1}\sum_{j=\pm1}\sum_{i=\pm1}(ijk)\,\mathrm{arctanh}\left[\frac{x-iM_x}{r(i,j,k)}\right], \tag{A.2}$$

$$B_z(x,y,z) = -\frac{1}{B_0}\sum_{k=\pm1}\sum_{j=\pm1}\sum_{i=\pm1}(ijk)\,\arctan\left[\frac{(x-iM_x)\,(y-jM_y)}{(z-kh)\,r(i,j,k)}\right] \tag{A.3}$$

Here $r(i,j,k) = \left[(x-iM_x)^2+(y-jM_y)^2+(z-kh)^2\right]^{1/2}$ and B_0 is such that $B_z(0,0,0)=1$. This follows from an integral over the region $\Omega = \{|x|\le M_x, |y|\le M_y, h\le|z|\le\infty\}$

Table A.2: The properties of the three magnets contributing to the magnetic field imposed in the numerical simulations.

	Magnet 1	Magnet 2	Magnet 3
(M_x, M_y, h)	$(0.04, 0.084, 0.04)$ m	$(0.042, 0.08, 0.04)$ m	$(0.04, 0.084, 0.04)$ m
(x_c, y_c, z_c)	$(-0.078, -0.15, 0.01)$ m	$(0.0, -0.15, 0.01)$ m	$(0.078, -0.15, 0.01)$ m
B_{face}	-0.55 T	0.65 T	-0.55 T

of magnetic dipoles, i.e., two magnets of dimensions $2M_x \times 2M_y$ separated by $2h$, connected by a soft core.

In the present work, three magnets are positioned on one side of the cavity. Therefore, the summation over $k = +1$ can be omitted from above summation, wheres the summation is carried out over three separate magnets, with their origin in (x_c, y_c, z_c) and certain magnitude. The resulting properties for the magnets are summarized in table A.2. As the magnets are positioned on one side, the normalization of the magnetic field was handled with respect to the face of the magnet, rather than the origin.